ROYAL SOCIETY
OF CHEMISTRY

PAPER

CrossMark
click for updates

Magnéli phase Ti_8O_{15} nanowires as conductive carbon-free energy materials to enhance the electrochemical activity of palladium nanoparticles for direct ethanol oxidation†

Pei Kang Shen,*[ab] Chunyong He,[c] Shiyong Chang,[d] Xiangdong Huang[d] and Zhiqun Tian[a]

Pure single-crystalline Magnéli phase Ti_8O_{15} nanowires (NWs) have been successfully synthesized via a facile one-step evaporation–deposition synthesis method in a hydrogen atmosphere. The electrical conductivity of a single Ti_8O_{15} nanowire is 2060 S m^{-1} at 300 K, which is much higher than that of carbon black ($\sim$100 S m^{-1}) and almost as high as that of graphite ($\sim$1000 S m^{-1}) or graphene ($\sim$2000 S m^{-1}). Pd nanoparticles (NPs) loaded on Ti_8O_{15} nanowires are synthesized through a pulsed electrodeposition method. As carbon-free support materials for Pd NPs, the Pd/Ti_8O_{15} NWs show a significantly enhanced activity for the ethanol oxidation reaction and excellent durability compared to the Pd/C catalyst. The peak current density of the Pd/Ti_8O_{15} NWs after 2000 cycles is 2791 mA mg$_{Pd}^{-1}$, with only 18.6% loss, while, on the Pd/C electrode, only a current density of 682 mA mg$_{Pd}^{-1}$ is observed, with a loss of 42.3% of the initial ethanol oxidation reaction activity. The synthetic approach for pure single-crystalline Magnéli phase Ti_8O_{15} nanowires gives the inspiration for the development of conductive carbon-free materials for electrocatalysis in direct alcohol fuel cells (DAFCs).

Introduction

TiO_2 shows promising applications in environmental remediation, solar energy conversion and other electrochemical energy storage devices[1–5] since it has no light corrosion, good acidic and alkaline resistance, stable chemical properties, and biological non-toxicity and is an abundant source. Therefore, the synthesis of TiO_2 has attracted significant attention in the past decade. However, TiO_2 is a type of wide band-gap semiconductor and it only adsorbs ultraviolet light, leading to low solar photovoltaic conversion efficiency, which greatly limits its practical applications in solar energy conversion.[6] In addition, TiO_2 also has a disadvantage of the realization of its applications in electrochemical energy storage devices, mainly due to its low electrical conductivity. Narrowing the band gap of TiO_2 to extend its electronic properties, which is the so-called band-

gap engineering, is an effective approach to improve its inherent shortcomings. Doping TiO_2 with metal or non-metal elements is known to be a feasible approach to tune the electronic structure of TiO_2, which leads to new states of TiO_2 for visible light response and performance improvements in electrochemical energy storage.[7–10] The other efficient approach is introducing oxygen vacancies or Ti^{3+} in TiO_2 to form reduced TiO_2, black TiO_2 or Magnéli phase Ti_nO_{2n-1} ($3 \leq n \leq 10$). These materials can tune the electronic structure of TiO_2 as well and introduce new states into the TiO_2 band gap. Therefore, these materials have been generally used as visible light-absorptive catalysts, or catalyst supports and battery electrode materials owing to their high electrical conductivity and unique composition and structures.[11–15]

Although the fabrication of shape-controlled TiO_2 nanoarchitectures has been studied extensively, the synthesis of shape-controlled Magnéli phase Ti_nO_{2n-1} nano-architectures is still a great challenge. Traditionally, Magnéli phase Ti_8O_{15} is synthesized by the thermal reduction of TiO_2 powder at high temperature with H_2 gas or other reductants.[16–18] However, this two-step synthesis strategy inevitably leads to the agglomeration of nanoparticles.[19] Although there have been some reports on the successful synthesis of black TiO_2 nanowires[20] or nanotubes[21] via hydrogenation, the direct synthesis of shape-controlled Magnéli phase Ti_nO_{2n-1} nano-architectures in one step is still a big challenge.

[a]Collaborative Innovation Center of Sustainable Energy Materials, Guangxi University, Nanning, Guangxi, 530004, PR China. E-mail: pkshen@gxu.edu.cn

[b]State Key Laboratory of Optoelectronic Materials and Technologies, School of Physics and Engineering, Sun Yat-sen University, Guangzhou, 510275, PR China

[c]Dongguan Institute of Neutron Science (DINS), Dongguan Branch, Institute of High Energy Physics, Chinese Academy of Sciences, Dongguan 523800, PR China

[d]Automotive Engineering Institute, Guangzhou Automobile Group Co., Ltd, Guangzhou, 510640, PR China

† Electronic supplementary information (ESI) available. See DOI: 10.1039/c5ta02622a

Direct alcohol fuel cells (DAFCs), which have been attracting an enormous amount of research interest, are considered to be one of the most promising devices for stationary and portable electronic applications owing to their high energy density, fuel portability, and low operating temperature.[22–24] Carbon-supported Pt or Pd based catalysts have been studied and applied as electrocatalysts in DAFCs.[25–27] However, due to the electrochemical corrosion of the carbon supporting material, the durability of carbon-supported catalysts is not able to meet the requirements for commercialized electrocatalysts in DAFCs.[28] Accordingly, persistent efforts have been made to explore carbon-free supporting materials in the past decades, including nitride,[29] carbide,[30] hollow-silica-spheres,[31] and as well as metal oxides.[32,33] Owing to its superb electrochemical durability, TiO_2 has been considered as a potential support for precious metal nanoparticles.[34,35] However, its intrinsic low electrical conductivity greatly restricts its applications.

Herein, we present a facile one-step evaporation–deposition route to pure single-crystalline Magnéli phase Ti_8O_{15} NWs as conductive carbon-free support materials for Pd NPs as efficient electrocatalysts in DAFCs. This simple strategy leads to great inspiration for synthesizing conductive shape-controlled transition metal oxides and utilizing them as active and low-cost catalysts or catalyst supports in electrochemical energy storage devices. The Pd/Ti_8O_{15} NWs showed significantly enhanced electrocatalytic performance and outstanding durability for ethanol oxidation.

Experimental

Synthesis of Ti_8O_{15} nanowires

Experimentally, the Ti_8O_{15} NWs were grown on a Ti foil (Grade 1, purity 99.5%) substrate; the size of the Ti foil substrate was 2.5 cm × 3.0 cm × 0.5 mm (width × length × thickness). Before evaporation–deposition, the Ti foil was chemically polished with HF : HNO_3 : H_2O (1 : 3 : 6) solution for 5 s to remove the surface impurities and then ultrasonically cleaned in acetone, ethanol and deionized water for 10 min, respectively. Pure TiO_2 powder (99.0%, 5–10 nm, 2 g) was placed into a quartz boat and the quartz boat was placed at the center of a conventional tube furnace (high temperature region, H.T.), while the Ti substrate was located downstream, 6 cm from the quartz boat (low temperature region, L.T.). Before the injection of H_2, the reaction system was flushed with N_2 (50 mL min^{-1}) for 1 h to remove residual oxygen and moisture, then, the tube was inflated with H_2 (20 mL min^{-1}) for 30 min. And subsequently, the furnace was heated to 1050 °C at a rate of 8 °C min^{-1} and maintained for 2 h with a hydrogen gas flow rate of 20 mL min^{-1}. Finally, the furnace was cooled at a rate of 5 °C min^{-1} down to room temperature and a layer of black material was observed on the surface of the Ti substrate (inset in Fig. 2a).

Preparation of Pd/Ti_8O_{15} NW electrocatalysts

The Pd/Ti_8O_{15} NW electrocatalyst was synthesized by pulsed electrodeposition of Pd NPs on Ti_8O_{15} NWs (acting as working electrode), which was carried out in a thermostat-controlled standard three-electrode electrochemical cell using a computerized potentiostat (Bio-logic VMP3, France). A saturated calomel electrode (SCE) acted as the reference electrode and a piece of platinum plate electrode (1 × 1 cm^{-2}) as the counter electrode. For the electrodeposition of Pd, 3 mmol L^{-1} Na_2PdCl_4 was formulated in 0.5 M H_2SO_4 as precursors. The deposition electrolyte was saturated with argon gas during the deposition processes with magnetic stirring. The potential imposed on the electrode was −1.6 V for 0.1 s (pulse nucleation) and a pulse of −0.2 V, corresponding to the nuclei growth for periods of 500 s. Subsequently, the Pd/Ti_8O_{15} NWs were thoroughly rinsed with deionized water several times.

Preparation of Pd/C electrocatalysts

The Pd/C catalyst was prepared via adsorption/reduction by an IMH method described as follows. The palladium(II) sodium chloride precursor (7.2 mL, 9.2 mg_{Pd} mL^{-1}) was well mixed with ethylene glycol (EG, 50 mL) in an ultrasonic bath. Then, VC-72 (100 mg) was added to the mixture. The pH of the mixture was adjusted to 10 with 0.1 mol L^{-1} NaOH/EG solution. After agitation and ultrasonication for 30 min, the mixture was microwave-heated in the process of 5 s-on/5 s-off for 20 times. The resulting black solid sample was acidified, filtered, washed and dried at 80 °C for 12 h in a vacuum oven.

Materials characterization

X-ray diffraction (XRD) analysis was carried out on a D8 ADVANCE powder X-ray diffractometer (Cu Kα, 30 kV, 30 mA). Scanning electron microscopy (SEM) was performed on a thermal field emission environmental SEM-ED-EBSD (Quanta 400F, FEI, Oxford, HKL Ltd.). High-resolution transmission electron microscopy (HRTEM) and high-angle annular dark-field scanning transmission electron microscopy-energy dispersive spectroscopy HAADF-STEM-EDS elemental mapping were performed using a Tecnai G2 F30 (FEI) operating at 300 kV. The X-ray photoelectron spectroscopy (XPS) measurements were carried out on an XPS apparatus (ESCALAB 250, Thermo-VG Scientific Ltd.). The loadings of Pd were measured using inductively coupled plasma-atomic emission spectrometry (ICP-AES (IRIS(HR)), USA). X-band electron paramagnetic resonance (EPR) spectra of the samples were collected at liquid nitrogen temperature using a electron paramagnetic resonance spectrometer (A300-10-12, BRÜCKNER).

To measure the conductivity under conditions of low energy and bias voltages, a voltage ramp of 0–0.05 V was applied across split electrodes in steps of 0.025 V for two-probe measurements using a source meter (Keithley 2400).

Electrochemical measurements

The electrocatalytic properties of Pd/Ti_8O_{15} NWs, represented by the catalytic oxidation of ethanol in DAFCs, were probed on an Bio-logic VMP3 electrochemical workstation in a thermostat-controlled standard three-electrode cell at 30 °C with a Hg/HgO (1.0 mol L^{-1} KOH) electrode as the reference electrode and a platinum foil (1.0 × 1.0 cm^{-2}) as the counter electrode. The ethanol oxidation reaction on the Pd/Ti_8O_{15} NW electrocatalyst

This journal is © The Royal Society of Chemistry 2015

J. Mater. Chem. A, 2015, **3**, 14416–14423 | **14417**

was carried out in a nitrogen-saturated 1.0 mol L^{-1} KOH + 1.0 mol L^{-1} CH$_3$CH$_2$OH solution. The cyclic voltammograms (CVs) were recorded at a scan rate of 20 mV s^{-1} within the potential window of -0.96 to 0.24 V vs. Hg/HgO. The durability of the Pd/Ti$_8$O$_{15}$ NWs for MOR was measured by performing CV of Pd/Ti$_8$O$_{15}$ NWs over 2000 cycles with the scan rate of 0.1 V s^{-1} and from -0.96 V to 0.24 V.

Platinum on a carbon catalyst (46.7 wt% Pt from TKK, Japan) was also measured for comparison. The catalyst ink was prepared as follows. 5.0 mg catalysts (Pd/C or Pt/C) and 0.5 mL Nafion solution (0.05 wt%, DuPont, USA) solution were dispersed in 0.5 mL of ethanol by sonication for an hour to form a well-dispersed ink. A certain amount of the ink was transferred onto the surface of a glassy carbon electrode. After drying under an infrared lamp for 5 min, a catalyst thin film was obtained.

The measured loadings of Pd on the Pd/Ti$_8$O$_{15}$ NW electrode were 0.078 mg cm^{-2}. And we kept the same metal loading on Pd/C and Pt/C electrodes.

Results and discussion

The product on the Ti substrate was collected and characterized by XRD. For comparison, the anatase TiO$_2$, rutile TiO$_2$ powder and the Ti substrate were also characterized as shown in Fig. 1a. The diffraction pattern of the product reveals a single phase of Ti$_8$O$_{15}$. Fig. 1b shows the enlarged XRD pattern of the product in the 2θ range of 25° to 45°. The identified peaks in the spectrum are indexed to triclinic Ti$_8$O$_{15}$ (JCPDF no. 50-0790).

Fig. 2 shows the morphology and structure of the as-prepared Ti$_8$O$_{15}$ NWs. Fig. 2a shows the typical plane-view SEM image of the Ti$_8$O$_{15}$ NWs on the Ti substrate. The inset in Fig. 2a is a digital photo of the sample, which reveals that a black layer is grown on the surface of the Ti substrate. Fig. 2b and c show the high magnification SEM images of the Ti$_8$O$_{15}$ NWs, indicating the highly uniform and densely packed array of the nanowires. They reveal an interconnected network, forming a highly hierarchically porous surface morphology. We also investigated the structures of the Ti$_8$O$_{15}$ NWs with HRTEM and selected area electron diffraction (SAED). Fig. 2d and e display the representative low-resolution TEM images of Ti$_8$O$_{15}$ NWs. The size of individual Ti$_8$O$_{15}$ NWs was approximately 30 nm in

diameter. The typical SEAD pattern in Fig. 2e (inset at the top right corner) was taken for a typical individual nanowire (marked by the red circle at the head of the nanowire); the regularly arranged spots show that the nanosheet is single crystal in nature. The pure Ti$_8$O$_{15}$ NWs were highly crystallized, as observed from the well-resolved lattice features shown in the HRTEM image (Fig. 2f). Two lattice plane distances of 0.315 nm and 0.281 nm can be clearly seen, corresponding to the $[\bar{1}2\bar{1}]$ and $[1\bar{2}\bar{7}]$ planes of Ti$_8$O$_{15}$.

High-angle annular dark-field scanning transmission electron microscopy (HAADF-STEM) analysis and X-ray elemental analysis were carried out to further analyze the structure and investigate the composition of Ti$_8$O$_{15}$ NWs, as shown in Fig. S1†. Fig. S1a† shows the HAADF-STEM image of a typical individual Ti$_8$O$_{15}$ nanowire, which clearly corroborates the TEM images. The distribution of elements in Ti$_8$O$_{15}$ NWs was observed using the HAADF-STEM-EDS maps (dotted box in Fig. S1a†). Ti and O are uniformly distributed in the Ti$_8$O$_{15}$ NWs. A line-profile analysis using HAADF-STEM-EDS was applied to analyze the chemical microstructure of the Ti$_8$O$_{15}$ NWs (Fig. S1d†), whose results are in accordance with the TEM results. Fig. S1e† displays the EDS pattern of Ti$_8$O$_{15}$ NWs.

In order to elucidate the chemical bonding on the Ti$_8$O$_{15}$ NWs and the absence of Ti^{3+}, we have further carried out X-ray photoelectron spectroscopy (XPS) (Fig. S2†). The comparison of the Ti-2p XPS spectra of Ti$_8$O$_{15}$ NWs and TiO$_2$ (Fig. S2a†) shows that the Ti$_8$O$_{15}$ NWs and TiO$_2$ have different features. TiO$_2$ shows typical Ti^{4+} features with the Ti 2p$_{3/2}$ peak centered at 458.6 eV and the Ti 2p$_{1/2}$ peak centered at 464.4 eV.[36,37] While Ti$_8$O$_{15}$ NWs display two additional small shoulder peaks centered at 463.7 and 458.0 eV, which are the characteristic feature of Ti-2p$_{1/2}$ and Ti-2p$_{3/2}$ peaks for the Ti^{3+} ions.[38] The O 1s core-level XPS spectra show that both the Ti$_8$O$_{15}$ NWs and TiO$_2$ have similar O 1s peaks centered at 530.1 eV, which is related to Ti–O–Ti (Fig. S2b†).[39] An additional peak at 532.0 eV in Ti$_8$O$_{15}$ NWs is assigned to the Ti–OH bond, which is attributed to the hydrogen atmosphere.[40] Electron paramagnetic resonance
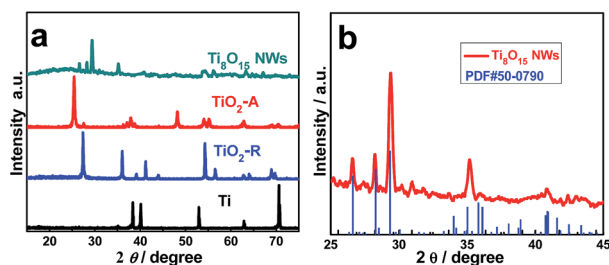

Fig. 1 (a) XRD pattern collected from the Ti$_8$O$_{15}$ NW product, anatase TiO$_2$ (TiO$_2$-A), rutile TiO$_2$ (TiO$_2$-R) and the Ti substrate and (b) enlarged XRD pattern of Ti$_8$O$_{15}$, the blue vertical lines indicate the peaks of the pure Ti$_8$O$_{15}$ reflections (JCPDF no. 50-0790).
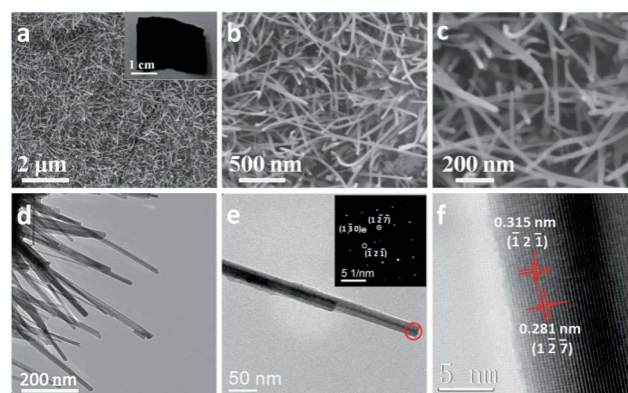

Fig. 2 Morphology and structure of the Ti$_8$O$_{15}$ NWs. (a) Typical SEM image of the Ti$_8$O$_{15}$ NWs on the Ti substrate, the inset in (a) is the digital image of the product, (b and c) high magnification SEM images of the Ti$_8$O$_{15}$ NWs, (d and e) TEM images of the Ti$_8$O$_{15}$ NWs, the inset in (e) is the corresponding selected area electron diffraction (SAED), and (f) HRTEM image of Ti$_8$O$_{15}$ NWs.

14418 | J. Mater. Chem. A, 2015, 3, 14416–14423

This journal is © The Royal Society of Chemistry 2015

(EPR) spectroscopy, as shown in Fig. 3, sheds more light on the electronic structure of Ti_8O_{15} NWs and TiO_2. TiO_2 does not show any active ESR signal, suggesting that it is free of $O_2^{\cdot}$ radicals or Ti^{3+} species. While Ti_8O_{15} NWs display an EPR resonance at $g = 1.98$, indicative of surface Ti^{3+}.[41] This spectral assignment is in accordance with our XPS data: some Ti^{3+} is present in Ti_8O_{15} NWs while only Ti^{4+} is present in TiO_2.

Fig. S3† presents the current–voltage (I–V) characteristics of one Ti_8O_{15} nanowire. The inset in Fig. S3† is the schematic diagram of the conductivity measurement. For the two-probe measurement, the linearity of the I–V characteristics was maintained by applying an appropriate low voltage/current. The dissipative power was kept under 1×10^{26} W to eliminate self-heating effects. The electrical conductivity of a single Ti_8O_{15} nanowire was 2060 S m^{-1} at 300 K obtained through calculation.

Since the Ti_8O_{15} NWs are grown under a H_2 atmosphere in the absence of catalysts, the growth mechanism of Ti_8O_{15} NWs cannot be dominated by the vapor–liquid–solid (VLS) mechanism, which is frequently employed to explain the growth of nanowires and nanoarchitectures.[42,43] With this in mind, we propose a modified vapor–solid (VS) mechanism to illustrate the growth mechanism of Ti_8O_{15} NWs.[44] In a typical VS process, the gas phase reactants were transferred from the high temperature region to the low temperature region and directly deposited on the substrate to form nanowires in the low temperature region.[45] The growth process of the Magnéli phase Ti_8O_{15} nanowires is presented in Scheme 1b. The pre-treatment of the Ti foil substrate leads to the formation of a layer of titanium oxide film (the left SEM image in Scheme 1c). When the temperature increases to 1050 °C, a two-step pathway reaction process was proposed in our synthesis process of Ti_8O_{15} NWs, shown as follows.

(1) The TiO_2 powder in the quartz boat in the high temperature region (H.T.) was reduced to form H_2O (g);

$$TiO_2 + H_2 \xrightarrow{\text{H.T.}} TiO_x + H_2O \text{ (g)}$$
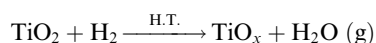
(2) The H_2O (g) reacted with the Ti on the Ti substrate (the low temperature region, L.T.) to form oxygen-deficient pure
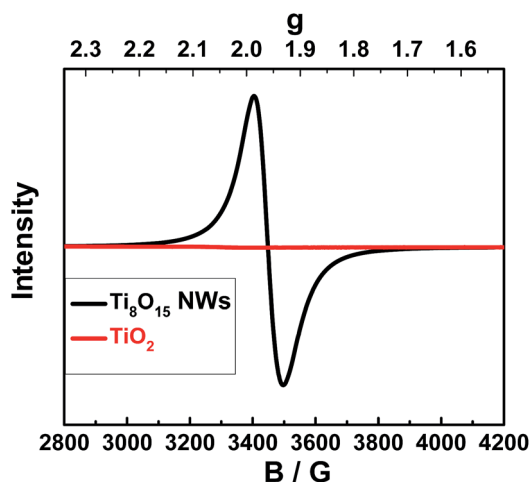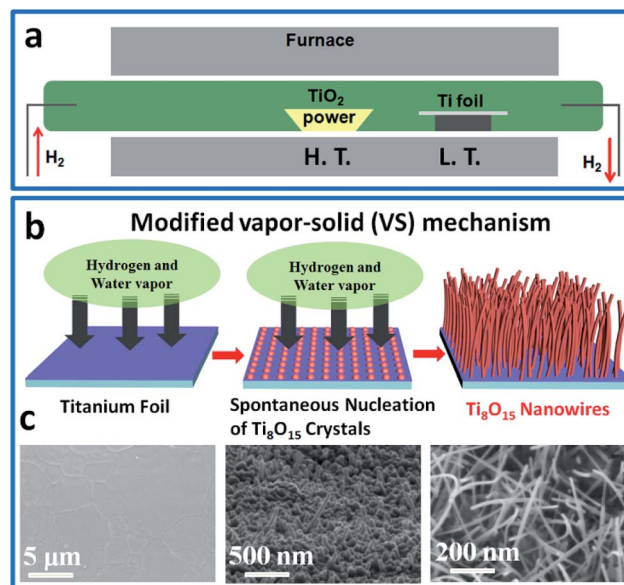

Scheme 1 (a) Schematic diagram of the experimental apparatus for the growth of Ti_8O_{15} NWs, the temperature decreases gradually from the centre to the right, resulting in two temperature regions: high (H.T.) and low temperature (L.T.), (b) schematic illustration of the modified VS process for Ti_8O_{15} NW growth and (c) corresponding SEM images of the Ti substrate at three different stages.

single-crystalline Magnéli phase of Ti_8O_{15} NWs in a H_2 atmosphere.

$$H_2O \text{ (g)} + Ti + H_2 \text{ (g)} \xrightarrow{\text{L.T.}} Ti_8O_{15} \text{ (NWs)} + H_2 \text{ (g)}$$
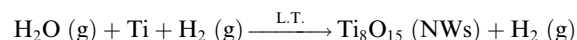
In the nucleation stage of the growth of the Ti_8O_{15} NWs, a layer of compact Ti_8O_{15} club-shaped nanoparticles was formed on the Ti foil substrate (the middle SEM image Scheme 1c). At the stage for heat treatment, as time goes on and upon continuous supply of reactants, the crystal nucleus continues to grow to Ti_8O_{15} NWs (the right SEM image in Scheme 1c).

The Magnéli phase Ti_8O_{15} nanowires were used as a carbon-free support to prepare Pd-based electrocatalysts (Pd/Ti_8O_{15} NWs) by a pulsed electrodeposition method. Fig. S4† displays the XRD pattern of Pd/Ti_8O_{15} NWs, showing the Pd and Ti_8O_{15} phases unambiguously. As shown in Fig. S4,† the peaks at 40°, 46°, 68° and 81° are assigned to the diffraction of the (111), (200), (220) and (311) crystal planes of the face centered cubic (fcc) structured Pd (JCPDS no. 46-1043), respectively. The other peaks between 25° and 37.0° correspond to the diffraction of Ti_8O_{15}.

Fig. 4a shows a typical bright-field TEM image of the Pd NPs deposited on Ti_8O_{15} NWs. The Pd NPs demonstrate a porous interconnected morphology of relatively uniform size distribution and good dispersion on the Ti_8O_{15} NW surface. The lattice fringes of the Ti_8O_{15} (105) plane and the Pt (111) plane are shown in Fig. 4b and c, respectively, indicating the formation of polycrystalline Pd NPs on the Ti_8O_{15} NW surface. These TEM images reveal that the Pd NPs (average size of ~3.5 nm) are interconnected and adhere to the Ti_8O_{15} NW surface (Fig. 4g), producing a polycrystalline Pd structure. Fig. 4d shows the

Fig. 3 Comparison of EPR spectra of TiO_2 and Ti_8O_{15} NWs.

HAADF-STEM image of Pd/Ti_8O_{15} NWs, confirming the porous interconnected morphology of Pd/Ti_8O_{15} NWs. The elemental mapping analysis of Ti and Pd using HAADF-STEM-EDS, obtained from the red box in Fig. 4d, reveals the uniform distribution of the Ti and Pd components in the nanocomposite (Fig. 4e and f), confirming the results of the HRTEM and HAADF-STEM analyses. Fig. 4h presents the EDS pattern of Pd/Ti_8O_{15} NWs, the co-existence of Ti, O and Pd further confirms the above results.

The catalytic properties of the as-prepared Pd/Ti_8O_{15} NWs were investigated for the direct ethanol oxidation reaction. For comparison, the ethanol oxidation reaction activities of Pd/C and Pt/C were also investigated under the same conditions. The cyclic voltammograms (CVs) of the Pd/C, Pd/Ti_8O_{15} NWs and Pt/C in N_2-saturated 1.0 mol L^{-1} KOH with a scan rate of 20 mV s^{-1} at 30 °C were recorded as shown in Fig. 5a. The Pd/Ti_8O_{15} NWs appear to have similar columbic features compared to the Pd/C. Three potential peaks were observed in the anodic scan, which correspond to different electrochemical processes occurring over the Pd surface: (1) the peak (Region A) that appeared at potentials lower than −0.75 V is associated with the oxidation of absorbed and desorbed hydrogen (Pd − $H_{abs/ads}$ + OH^- → Pd + H_2O + e^-); (2) the peak (Region B) occurring at a potential of ∼−0.4 V is related to the adsorption of hydroxyl groups (Pd + OH^- ↔ Pd − OH_{ads} + e^-); (3) the peak (Region C) occurring at potentials above −0.2 V can be attributed to the formation of the palladium(II) oxide layer on the surface of the catalyst (Pd − OH_{ads} + OH^- ↔ Pd − O + H_2O + e^-).[46] In the cathodic scan, a peak (Region D) centered at about −0.23 V was observed, which is associated with the reduction of Pd (Pd − O + H_2O + $2e^-$ ↔ Pd + $2OH^-$) and Region E corresponds to the absorption of hydrogen.

To evaluate the electrocatalytic activity of Pd/Ti_8O_{15} NWs, the ethanol oxidation reaction has been carried out in 1.0 mol L^{-1} KOH. A comparison of the CVs recorded for the Pd/C, Pd/Ti_8O_{15} NWs and Pt/C at 50 mV s^{-1} in 1.0 mol L^{-1} KOH + 1.0 mol L^{-1} CH_3CH_2OH solution is shown in Fig. 5b. The observed voltammetric curves are excellent signatures of ethanol oxidation at all three electrodes. The Pd/Ti_8O_{15} NWs showed enhanced electrocatalytic activity compared to Pd/C and Pt/C counterparts: the Pd/Ti_8O_{15} NWs exhibit a more negative onset potential (−0.543 V vs. Hg/HgO) than those of Pd/C (−0.451 V vs. Hg/HgO) and Pt/C (−0.490 V vs. Hg/HgO) alone with higher peak current densities (3430 mA mg_{Pd}^{-1}) compared to Pd/C (1194 mA mg_{Pd}^{-1}) and Pt/C (1853 mA mg_{Pt}^{-1}). The onset potential (E_{onset}) describes the ease at which electro-oxidation occurs at the catalyst, thus it should be more negative for the best-performing electrocatalysts for the ethanol oxidation reaction. The Pd/Ti_8O_{15} NWs exhibit a 2.9- and 1.8-fold enhancement in mass activity compared to the Pd/C and Pt/C, respectively. The above results show that the Pd/WC_P/G catalyst exhibits the best electro-oxidation activity toward ethanol among the three catalysts. The reaction activation free energy ($\Delta G°$) is related to the activities of the catalysts. A lower $\Delta G°$ corresponds to a higher activity. The lower $\Delta G°$ value of 24.6 J mol^{-1} was obtained for the ethanol oxidation on Pd/Ti_8O_{15} NWs as compared to 35.2 J mol^{-1} on Pd/C, indicating improved kinetics (Fig. S5†).

The mechanism of the ethanol oxidation reaction is complicated as it involves the generation of several intermediate products (such as linearly adsorbed CO and adsorbed CH_x species) and final products (such as CO_2, acetaldehyde and acetic acid).[47–49] So, one major problem concerning ethanol oxidation on noble metals is the adsorption of poisoning intermediates, which leads to the deactivation of the electrode surface for further oxidation. A steady-state measurement was used to evaluate the level of the electrode surface contamination with adsorbed poisoning carbonaceous species. The respective chronopotentiometric curves for ethanol oxidation on Pd/C, Pd/Ti_8O_{15} NWs and Pt/C electrodes at a current density of 5 mA cm^{-2} are shown in Fig. 6a. The potential oscillation appeared on the Pt/C electrode after 546 seconds of constant current
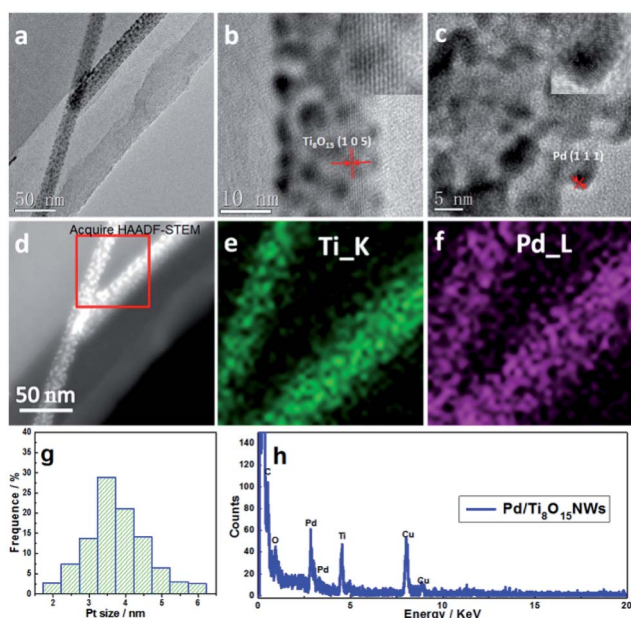

Fig. 4 Morphology and structure of the Pd/Ti_8O_{15} NWs. (a) TEM image of Pd/Ti_8O_{15} NWs, (b and c) HRTEM images of Pd/Ti_8O_{15} NWs, insets are the corresponding enlarged images, (d) HAADF-STEM image of Pd/Ti_8O_{15} NWs, the corresponding elemental mapping for titanium (e) and palladium (f) in Pd/Ti_8O_{15} NWs obtained from the red box in (d), (g) the corresponding size-distribution histograms of the Pd NPs and (h) EDS pattern of Pd/Ti_8O_{15} NWs.
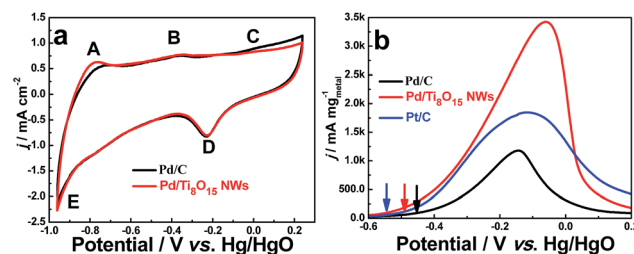

Fig. 5 (a) Typical cyclic voltammograms (CVs) of Pd/C and Pd/Ti_8O_{15} NWs in N_2-saturated 1.0 mol L^{-1} KOH with a scan rate of 20 mV s^{-1} at 30 °C and (b) CVs recorded at 50 mV s^{-1} of Pd/C, Pd/Ti_8O_{15} NWs and Pt/C in 1.0 mol L^{-1} KOH + 1.0 mol L^{-1} CH_3CH_2OH solution.

14420 | J. Mater. Chem. A, 2015, 3, 14416–14423

This journal is © The Royal Society of Chemistry 2015

polarization, indicating the deterioration and poisoning due to the adsorption of poisonous species on the surface of platinum, which need higher potentials to oxidize the adsorbed poisonous species and release a clean surface.[50,51] The chronopotentiometric curves for ethanol oxidation on Pd/C and Pd/Ti$_8$O$_{15}$ NWs are smooth. The potential to satisfy the applied anodic current density on Pd/Ti$_8$O$_{15}$ NWs is lower than that of Pd/C and Pt/C, lower potential means higher output voltage and power density, which indicates that ethanol oxidation on Pd/Ti$_8$O$_{15}$ NWs occurs *via* a more efficient pathway and no obvious poisonous species are found on the surfaces of the Pd/Ti$_8$O$_{15}$ NWs. The anti-poisoning ability of the catalyst can be characterized by the time (T) that the catalyst can sustain the activity for ethanol oxidation at low overpotential. As shown in Fig. 6a, the T values decrease in this order: Pd/Ti$_8$O$_{15}$ NWs (>3000 s) > Pd/C (2300 s) > Pt/C (1711 s). The above results prove that the Pd/Ti$_8$O$_{15}$ NW catalyst exhibits better electrocatalytic properties and better resistance to poisoning than the Pd/C and Pt/C catalysts. The application of traditional carbon-supported Pd-based catalysts in DAFCs is not only hindered by the electrochemical corrosion of the carbon supporting material, but also restricted by the deactivation of Pd NPs. The deactivation mechanism of the Pd-based catalysts in the process of DAFC operation is that gradual build-up of adsorbed poisonous species on the surfaces of the Pd blocks the catalytic active sites.[52]

The stability of the electrocatalysts under continuous operating conditions was further examined by chronoamperometric measurements. The chronoamperometry (CA) profiles for ethanol oxidation on Pd/C, Pd/Ti$_8$O$_{15}$ NWs and Pt/C at a potential of -0.15 V (*vs.* Hg/HgO) for 1600 s in 1.0 mol L^{-1} KOH + 1.0 mol L^{-1} CH$_3$CH$_2$OH solution are shown in Fig. 6b. As displayed in Fig. 6b, an initial rapid decrease in current density was observed for Pd/C and Pt/C electrodes, which could be ascribed to the accumulation of strongly adsorbed poisonous reaction intermediates on the surface active sites.[53] While on the Pd/Ti$_8$O$_{15}$ NW electrode, the initial descent of the current density is slow, which indicates that the deactivation caused by the adsorbed poisonous reaction intermediates on the Pd/Ti$_8$O$_{15}$ NW electrode is much lighter than that on Pd/C and Pt/C, which is consistent with the previous analysis. From Fig. 6b, we conclude that the activity order of the ethanol oxidation reaction in terms of the current density is Pd/Ti$_8$O$_{15}$
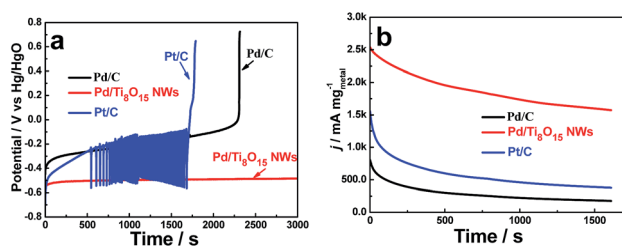
NWs > Pt/C > Pd/C. In particular, the Pd/Ti$_8$O$_{15}$ NWs exhibit 8.9- and 4.2-fold enhancement in mass activity compared to Pd/C and Pt/C after 1600 s of reaction, respectively.

The stability of the electrocatalysts under continuous operating conditions was further examined by continuous potentiodynamic sweep between -0.6 and 0.2 V (*vs.* Hg/HgO). Fig. 7a and b display the CVs for the ethanol oxidation reaction on Pd/Ti$_8$O$_{15}$ and Pd/C electrodes before and after 2000 cycles of the potentiodynamic sweep test. The peak current density of the Pd/Ti$_8$O$_{15}$ after 2000 cycles was 2791 mA mg$_{Pd}$$^{-1}$, with only an 18.6% loss. While, on the Pd/C electrode, only a current density of 682 mA mg$_{Pd}$$^{-1}$ was observed, with a loss of 42.3% of the initial ethanol oxidation reaction activity (Fig. 7c).

Based on the above results, the electrocatalytic performance and catalytic stability of the Pd/Ti$_8$O$_{15}$ NW electrode for the ethanol oxidation reaction in DAFCs are distinctly improved compared with Pd/C. First, oxygen vacancies/Ti^{3+} in Ti$_8$O$_{15}$ NWs generate a population of surface electrons available for conduction, and higher electron transfer efficiency can be achieved in the Pd/Ti$_8$O$_{15}$ NW electrode during the catalytic process, which enhances the ethanol oxidation reaction activity and durability.[54] Moreover, Ti$_8$O$_{15}$ NWs can change the hydroxyl/ethanol adsorption conditions, which is a predominant issue involved in the kinetics of the ethanol oxidation reaction,[46] through the change of the electronic structure of Pd, connected to the electronic interactions between Pd and the supporting material (Ti$_8$O$_{15}$ NWs). These interactions are to be expected since Ti$_8$O$_{15}$ NWs have a hypo-d-electron character and could have the ability to interact with Pd which also has a hyper-d-electron character.[55,56] This electronic interaction between Pd and Ti$_8$O$_{15}$ NWs leads to a higher catalytic activity of the OH$_{ads}$ state in the Pd surface, and then facilitates the interaction of Pd-(CH$_3$CO)$_{ads}$ with Pd-OH$_{ads}$ (Pd-(CH$_3$CO)$_{ads}$ + Pd-OH$_{ads}$ → Pd–CH$_3$COOH + Pd), increasing the activity of the catalyst for
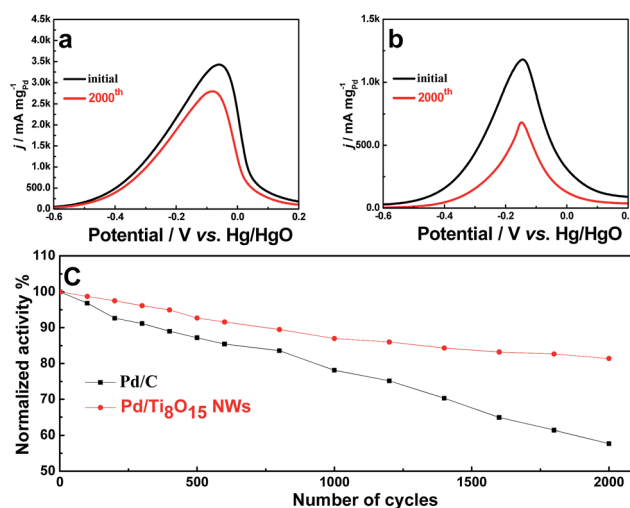

Fig. 7 Polarization curves for the ethanol oxidation reaction on (a) Pd/Ti$_8$O$_{15}$ NW and (b) Pd/C electrodes before and after the continuous CV cycling test in N$_2$-saturated 1.0 mol L^{-1} KOH + 1.0 mol L^{-1} CH$_3$CH$_2$OH solution and (c) comparison of the peak current density changing with cycle time for the Pd/C and Pd/Ti$_8$O$_{15}$ NWs.
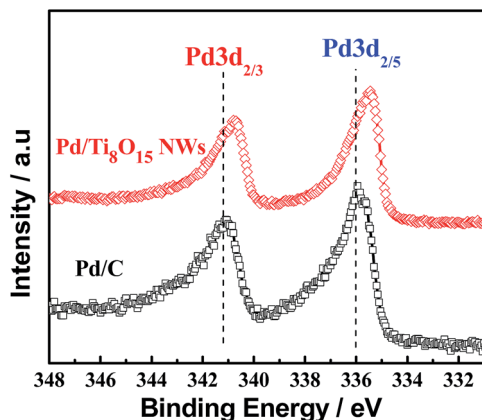

Fig. 6 (a) The chronopotentiometric curves of Pd/C, Pd/Ti$_8$O$_{15}$ NW and Pt/C catalysts at an anodic current density of 5 mA cm^{-2} and (b) chronoamperometric curves for the oxidation of ethanol catalyzed by Pd/C, Pd/Ti$_8$O$_{15}$ NWs and Pt/C at 0.3 V (*vs.* SCE) in N$_2$-saturated 1.0 mol L^{-1} KOH + 1.0 mol L^{-1} CH$_3$CH$_2$OH solution.

This journal is © The Royal Society of Chemistry 2015

J. Mater. Chem. A, 2015, **3**, 14416–14423 | **14421**

Fig. 8 XPS spectra of the Pd 3d region for Pd/C and Pd/Ti$_8$O$_{15}$ NWs.

the ethanol oxidation reaction.[57] In order to provide insight into the origin of the promotional effect of Pd/Ti$_8$O$_{15}$ NWs, XPS was applied to investigate the electronic structure of Pd in Pd/C and Pd/Ti$_8$O$_{15}$ NWs. Fig. 8 shows the comparison of the Pd 3d XPS spectra of Pd/C and Pd/Ti$_8$O$_{15}$ NWs. Compared to Pd/C, the Pd 3d peaks of Pd/Ti$_8$O$_{15}$ NWs shift, by about 0.6 eV, to a lower binding energy. The weakened 3d electron binding energy of Pd in Pd/Ti$_8$O$_{15}$ NWs is likely to result from the electronic interaction between the Pd and Ti$_8$O$_{15}$ NWs, which occurs through a partial electron transfer from Ti$_8$O$_{15}$ NWs to Pd. The electron transfer would increase the electron density of Pd and enhance the penetration of outer-layer electrons to the inner layer, which further down shifts the d-band center of Pd[58] and substantially enhances the activity toward the ethanol oxidation reaction.

Conclusions

In conclusion, we have successfully synthesized pure single-crystalline Magnéli phase Ti$_8$O$_{15}$ NWs through a facile one-step evaporation–deposition synthesis approach. A tentative modified vapor–solid (VS) mechanism was proposed in this work to illustrate the growth mechanism of Ti$_8$O$_{15}$ NWs. The electrical conductivity of a single Ti$_8$O$_{15}$ nanowire is 2060 S m^{-1} at 300 K, which is much higher than that of carbon black ($\sim$100 S m^{-1}) and almost as high as that of graphite ($\sim$1000 S m^{-1}) or graphene ($\sim$2000 S m^{-1}). Serving as a conductive carbon-free support material, Ti$_8$O$_{15}$ NWs were used to load Pd NPs to form Pd/Ti$_8$O$_{15}$ NWs. Compared with Pd/C, the Pd/Ti$_8$O$_{15}$ NWs showed a significantly enhanced activity for the ethanol oxidation reaction and outstanding durability, making it a possible candidate for the next generation electrocatalysts in DAFCs.

Acknowledgements

Notes and references

1 L. Li, J. Yan, T. Wang, Z.-J. Zhao, J. Zhang, J. Gong and N. Guan, *Nat. Commun.*, 2015, **6**, 5881.

2 Y. Ma, X. Wang, Y. Jia, X. Chen, H. Han and C. Li, *Chem. Rev.*, 2014, **114**, 9987–10043.

3 T. Xia, Y. Zhang, J. Murowchick and X. Chen, *Catal. Today*, 2014, **225**, 2–9.

4 S. Su, Z. Huang, Y. NuLi, F. Tuerxun, J. Yang and J. Wang, *Chem. Commun.*, 2015, **51**, 2641–2644.

5 K. Jukk, N. Kongi, A. Tarre, A. Rosental, A. B. Treshchalov, J. Kozlova, P. Ritslaid, L. Matisen, V. Sammelselg and K. Tammeveski, *J. Electroanal. Chem.*, 2014, **735**, 68–76.

6 X. Chen and S. S. Mao, *Chem. Rev.*, 2007, **107**, 2891–2959.

7 R. Asahi, T. Morikawa, T. Ohwaki, K. Aoki and Y. Taga, *Science*, 2001, **293**, 269–271.

8 M. Liu, X. Qiu, M. Miyauchi and K. Hashimoto, *J. Am. Chem. Soc.*, 2013, **135**, 10064–10072.

9 A. Kumar and V. Ramani, *ACS Catal.*, 2014, **4**, 1516–1525.

10 J. Zhang, T. Huang, L. Zhang and A. Yu, *J. Phys. Chem. C*, 2014, **118**, 25300–25309.

11 S. Hoang, S. P. Berglund, N. T. Hahn, A. J. Bard and C. B. Mullins, *J. Am. Chem. Soc.*, 2012, **134**, 3659–3662.

12 X. Chen, L. Liu, P. Y. Yu and S. S. Mao, *Science*, 2011, **331**, 746–750.

13 T. Ioroi, H. Senoh, S.-i. Yamazaki, Z. Siroma, N. Fujiwara and K. Yasuda, *J. Electrochem. Soc.*, 2008, **155**, B321–B326.

14 A. Kitada, G. Hasegawa, Y. Kobayashi, K. Miyazaki, T. Abe, K. Kanamori, K. Nakanishi and H. Kageyama, *RSC Adv.*, 2013, **3**, 7205–7208.

15 C. He, S. Chang, X. Huang, Q. Wang, A. Mei and P. K. Shen, *Nanoscale*, 2015, **7**, 2856–2861.

16 C. Acha, M. Monteverde, M. Nñúez-Regueiro, A. Kuhn and M. A. Alario Franco, *Eur. Phys. J. B*, 2003, **34**, 421–428.

17 Y. Lu, Y. Matsuda, K. Sagara, L. Hao, T. Otomitsu and H. Yoshida, *Adv. Mater. Res.*, 2011, **415–417**, 1291–1296.

18 A. Kitada, G. Hasegawa, Y. Kobayashi, K. Kanamori, K. Nakanishi and H. Kageyama, *J. Am. Chem. Soc.*, 2012, **134**, 10894–10898.

19 S. Perera, N. Zelenski and E. G. Gillan, *Chem. Mater.*, 2006, **18**, 2381–2388.

20 G. Wang, H. Wang, Y. Ling, Y. Tang, X. Yang, R. C. Fitzmorris, C. Wang, J. Z. Zhang and Y. Li, *Nano Lett.*, 2011, **11**, 3026–3033.

21 N. Liu, C. Schneider, D. Freitag, M. Hartmann, U. Venkatesan, J. Müller, E. Spiecker and P. Schmuki, *Nano Lett.*, 2014, **14**, 3309–3313.

22 X. Zhao, M. Yin, L. Ma, L. Liang, C. Liu, J. Liao, T. Lu and W. Xing, *Energy Environ. Sci.*, 2011, **4**, 2736–2753.

23 Z. Jiang, X. Zhao, Y. Fu and A. Manthiram, *J. Mater. Chem.*, 2012, **22**, 24862–24869.

24 M. C. Figueiredo, O. Sorsa, N. Doan, E. Pohjalainen, H. Hildebrand, P. Schmuki, B. P. Wilson and T. Kallio, *J. Power Sources*, 2015, **275**, 341–350.

14422 | *J. Mater. Chem. A*, 2015, **3**, 14416–14423

This journal is © The Royal Society of Chemistry 2015

25 S. Sun, G. Zhang, N. Gauquelin, N. Chen, J. Zhou, S. Yang, W. Chen, X. Meng, D. Geng, M. N. Banis, R. Li, S. Ye, S. Knights, G. A. Botton, T.-K. Sham and X. Sun, *Sci. Rep.*, 2013, **3**, 1775.

26 C.-H. A. Tsang, K. N. Hui, K. S. Hui and L. Ren, *J. Mater. Chem. A*, 2014, **2**, 17986–17993.

27 W. Yuan, Y. Cheng, P. K. Shen, C. M. Li and S. P. Jiang, *J. Mater. Chem. A*, 2015, **3**, 1961–1971.

28 Y.-J. Wang, D. P. Wilkinson and J. Zhang, *Chem. Rev.*, 2011, **111**, 7625–7651.

29 Y. Xiao, G. Zhan, Z. Fu, Z. Pan, C. Xiao, S. Wu, C. Chen, G. Hu and Z. Wei, *Electrochim. Acta*, 2014, **141**, 279–285.

30 M. K. Jeon, H. Daimon, K. R. Lee, A. Nakahara and S. I. Woo, *Electrochem. Commun.*, 2007, **9**, 2692–2695.

31 A. A. Melvin, V. S. Joshi, D. C. Poudyal, D. Khushalani and S. K. Haram, *ACS Appl. Mater. Interfaces*, 2015, **7**, 6590–6595.

32 B. Abida, L. Chirchi, S. Baranton, T. W. Napporn, H. Kochkar, J.-M. Léger and A. Ghorbel, *Appl. Catal., B*, 2011, **106**, 609–615.

33 M. S. Ide, D. D. Falcone and R. J. Davis, *J. Catal.*, 2014, **311**, 295–305.

34 K.-W. Park and K.-S. Seol, *Electrochem. Commun.*, 2007, **9**, 2256–2260.

35 S. J. Yoo, T.-Y. Jeon, K.-S. Lee, K.-W. Park and Y.-E. Sung, *Chem. Commun.*, 2010, **46**, 794–796.

36 X. Chen, L. Liu, Y. Y. Peter and S. S. Mao, *Science*, 2011, **331**, 746–750.

37 X. Chen and C. Burda, *J. Am. Chem. Soc.*, 2008, **130**, 5018–5019.

38 Z. Song, J. Hrbek and R. Osgood, *Nano Lett.*, 2005, **5**, 1327–1332.

39 G. Lu, S. L. Bernasek and J. Schwartz, *Surf. Sci.*, 2000, **458**, 80–90.

40 X. Lu, G. Wang, T. Zhai, M. Yu, J. Gan, Y. Tong and Y. Li, *Nano Lett.*, 2012, **12**, 1690–1696.

41 V. Etacheri, J. E. Yourey and B. M. Bartlett, *ACS Nano*, 2014, **8**, 1491–1499.

42 X. Duan and C. M. Lieber, *Adv. Mater.*, 2000, **12**, 298–302.

43 Y. Hao, G. Meng, Z. L. Wang, C. Ye and L. Zhang, *Nano Lett.*, 2006, **6**, 1650–1655.

44 Z. W. Pan, Z. R. Dai and Z. L. Wang, *Science*, 2001, **291**, 1947–1949.

45 J. Zhou, N. S. Xu, S. Z. Deng, J. Chen, J. C. She and Z. L. Wang, *Adv. Mater.*, 2003, **15**, 1835–1840.

46 Z. X. Liang, T. S. Zhao, J. B. Xu and L. D. Zhu, *Electrochim. Acta*, 2009, **54**, 2203–2208.

47 X. Fang, L. Wang, P. K. Shen, G. Cui and C. Bianchini, *J. Power Sources*, 2010, **195**, 1375–1378.

48 C. Bianchini and P. K. Shen, *Chem. Rev.*, 2009, **109**, 4183–4206.

49 M. B. Rohwer, R. M. Modibedi and K. I. Ozoemena, *Electroanalysis*, 2015, **27**, 1–8.

50 M. Krausa and W. Vielstich, *J. Electroanal. Chem.*, 1995, **399**, 7–12.

51 P. Justin and G. Ranga Rao, *Int. J. Hydrogen Energy*, 2011, **36**, 5875–5884.

52 X. Yu and P. G. Pickup, *Electrochem. Commun.*, 2009, **11**, 2012–2014.

53 W. Du, K. E. Mackenzie, D. F. Milano, N. A. Deskins, D. Su and X. Teng, *ACS Catal.*, 2012, **2**, 287–297.

54 F. Shi, L. R. Baker, A. Hervier, G. A. Somorjai and K. Komvopoulos, *Nano Lett.*, 2013, **13**, 4469–4474.

55 L. M. Vračar, N. V. Krstajić, V. R. Radmilović and M. M. Jakšić, *J. Electroanal. Chem.*, 2006, **587**, 99–107.

56 B. Babić, J. Gulicovski, L. Gajić-Krstajić, N. Elezović, V. R. Radmilović, N. V. Krstajić and L. M. Vračar, *J. Power Sources*, 2009, **193**, 99–106.

57 S. Neophytides, S. Zafeiratos, G. Papakonstantinou, J. Jaksic, F. Paloukis and M. Jaksic, *Int. J. Hydrogen Energy*, 2005, **30**, 393–410.

58 D. J. Ham, C. Pak, G. H. Bae, S. Han, K. Kwon, S.-A. Jin, H. Chang, S. H. Choi and J. S. Lee, *Chem. Commun.*, 2011, **47**, 5792–5794.

This journal is © The Royal Society of Chemistry 2015

J. Mater. Chem. A, 2015, **3**, 14416–14423 | **14423**